

Multiscale simulation of polymer melt spinning by using the dumbbell model

Takeshi Sato, Kazuhiro Takase and Takashi Taniguchi*

Department of Chemical Engineering, Kyoto University, Kyoto 615-8510, Japan

We investigated the spinning process of a polymeric material by using a multiscale simulation method which connects the macroscopic and microscopic states through the stress and strain-rate tensor fields, by using Lagrangian particles (filled with polymer chains) along the spinning line. We introduce a large number of Lagrangian fluid particles into the fluid, each containing N_p -Hookean-dumbbells to mimic the polymer chains ($N_p=10^4$), which is equivalent to the upper convected Maxwell fluid in the limit that $N_p \rightarrow \infty$. Depending on the Reynolds number Re , we studied the dynamical behaviors of fibers for the (a) $Re \rightarrow 0$ and (b) finite Re cases, for different draw ratios Dr , ranging from 10 to 30, and two typical Deborah numbers $De=10^{-3}$ and $De=10^{-2}$. In the limit $Re \rightarrow 0$ (a), as the Deborah number De increases, the elastic effect makes the system stable. At finite Re (b), we found that inertial effects play an important role in determining the dynamical behavior of the spinning process, and for $Dr=10^{-2}$ the system is quite stable, at least up to a draw ratio of $Dr=30$. We also found that the fiber velocity and cross section area are determined solely by the draw ratio. By comparing the velocity and cross section area profiles with the end-point distribution for the dumbbell connective vectors, for dumbbells located in Lagrangian particles along typical places along the spinning line, we show that our multiscale simulation method successfully bridges the microscopic state of the system with its simultaneous macroscopic flow behavior. It is also confirmed that the present schemes gives good agreements with the results obtained by the Maxwell constitutive equation.

KEYWORDS: Multiscale simulation, Melt spinning process, Viscoelastic fluids, Maxwell model dumbbell model

1. Introduction

Polymeric products have contributed to various industrial fields such as architecture, automotive, aerospace and medical fields. To produce the desired products, it is important to develop appropriate polymer processing technologies, whereby one can control the specific properties of these products. One of the most common methods to manufacture a polymeric fiber is the melt-spinning process (see Fig.1).¹⁻³ After the pioneering study of Kase and Matsuo^{4,5} for spinning processes of Newtonian fluids, a large number of theoretical and numerical studies on the process have been performed by many researchers.^{6-8,11-13,15-18} At present, the simulation techniques of melt spinning processes have been developed and applied to industrial problems, but there still remains unsolved problems, if specifically say, predictions of the microscopic state of polymer chains during spinning processes, such as the degree of orientation of polymer chains, position dependent entanglements density along a spinning line, entanglement distribution on a single polymer chain and crystallization of semi-crystalline polymer on spinning process.²¹ In most studies, a macroscopic approach using the Cauchy momentum equation with a constitutive equation to obtain the excess stress for the polymeric material has been commonly used. However, it has been recognized that the stress obtained by such a constitutive equation does not always predict the rheological properties of the target polymeric liquid correctly. One may consider to simply use a molecular dynamics method to solve the macroscopic flow problem, how-

ever, the numerical cost of such an approach is prohibitive. To overcome this problem, we propose and develop a MultiScale Simulation (MSS) method where the macroscopic model and microscopic molecular model are directly connected through the stress and strain rate tensor fields. This type of multiscale simulation method has been proposed by Öttinger with the concept of “CONNFESSIT”^{32,33}. In the MSS method of the present work, we introduce Lagrangian particles as fluid elements, each of which contains many molecules to precisely describe the microscopic states. So far, for flow problems of polymeric fluids a limited number of this type of multiscale simulations have been performed.³²⁻⁵⁰ Actually, the MSS method has been applied to solve flow problems of polymeric liquids in rather simple flow geometries such as flows in between two parallel plates^{33,35,36,41-47,50}, flows around an infinitely long cylinder,^{37,40,48,49} flows in between eccentric rotating cylinders^{38,39} and so forth. As far as we know, no one has ever attempted to apply this type of multiscale simulation method to an industrial polymer process before. This means that an MSS method applicable to industrial polymer processing problems has not yet been established. Hence, the aims of the present paper are (i) to develop an MSS method applicable to a polymer melt spinning process and (ii) to check the validity and efficiency of this method. To make the assessment of the MSS method easier, in the present work we select a rather simple microscopic model for the polymer chains, *i.e.*, a Hookean dumbbell model, because it is well-known that the stress given by a set of Hookean dumbbells is equivalent to the one evaluated by the upper convected Maxwell constitutive

*E-mail: taniguch@cheme.kyoto-u.ac.jp

equation, provided the number of dumbbells goes infinity. Although the dumbbell model is not a realistic polymer model, we will be able to apply the present method to a more realistic situation just by replacing the model with a elaborated polymer model such as PASTA^{28,29} or NAPLES²⁶, among many others.

The content of this paper is as follows. In the next section, we explain our model for the melt spinning process at the macroscopic and microscopic levels separately. In Sec. 2.1 we describe the governing equations at the macroscopic level, *e.g.*, the time evolution of the cross section area and the fiber velocity, with the appropriate boundary conditions, and the assumptions we have used. In Sec. 2.2 we describe the set of equations used to investigate the dynamics of the dumbbells in the microscopic model for the polymer chains. In Sec. 2.3 we explain how we have performed the multiscale simulations for a melt-spinning process as a function of the Reynolds number Re . In Sec. 3 the results for the (a) $Re \rightarrow 0$ and (b) finite Re cases are presented separately, and explained in detail. Finally, we give a summary in Sec. 4.

2. Melt spinning model

2.1 Equations of motion at the macroscopic level

Here we briefly explain the one dimensional model for a polymer melt spinning that we have used, even though such models have been previously developed by other researchers^{8–10, 12–15, 19}. A typical polymer melt spinning is drawn in Fig.1. A polymer melt is extruded from a die with a velocity V_o , and then the extrudate runs through the air. Finally the filament is taken up at a roll inside a water bath. In deriving the set of equations for the one dimensional model of a polymer melt spinning process, the following assumptions are made:

- (i) The shape of the filament is axi-symmetric.
- (ii) The polymer chains are relaxed at the place where the diameter of the extruded filament from the orifice shows a maximum due to the die swelling effect.
- (iii) The filament in the air gap region is isothermal.⁵¹
- (iv) The gravitational force, surface tension between the polymer melt and the air, and the friction of filament with the air are all neglected.
- (v) The polymer filament is in the melt state just before reaching the surface of the cooling-water, and just after it has gone into the water bath, it is solidified instantaneously by cooling.

Under the assumptions mentioned above, the dynamics of the melt spinning process at the macroscopic level can be described by the cross section area $A(x, t)$, the velocity $V(x, t)$ and the tension $F(x, t)$ of the filament at a position x and at time t . The time evolution equation of the cross section area $A(x, t)$ is given by the following equation of continuity :

$$\frac{\partial A(x, t)}{\partial t} = -\frac{\partial}{\partial x} (A(x, t)V(x, t)). \quad (1)$$

The tension of the fiber can be expressed as

$$F(x, t) = A(x, t)\sigma(x, t), \quad (2)$$

where σ is the normal stress difference defined by using the stress tensor of the polymer melt $\sigma_{\alpha\beta}$ ($\alpha, \beta \in \{x, y, z\}$) as

$$\sigma(x, t) = \sigma_{xx} - (\sigma_{yy} + \sigma_{zz})/2. \quad (3)$$

The equation for the velocity is given by

$$\rho A \frac{DV(x, t)}{Dt} = \frac{\partial}{\partial x} F(x, t), \quad (4)$$

where $D/Dt = \partial/\partial t + V\partial/\partial x$ is the Lagrangian derivative. Note

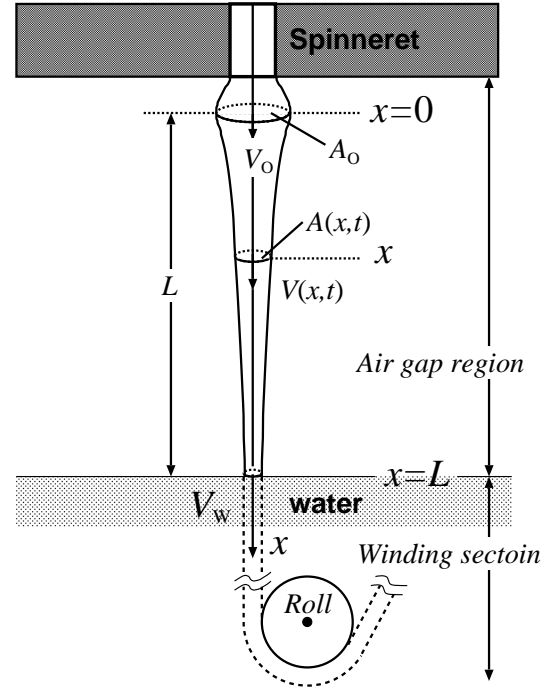


Fig. 1. Schematic view of the melt spinning process

that in an incompressible Newtonian fluid the uniaxial elongation stress σ is expressed as $\sigma = 3\eta_s \partial V / \partial x$, η_s being the shear viscosity of the fluid. The boundary conditions for A and V at $x=0$ are given as

$$V(x=0, t) = V_o \quad \text{and} \quad A(x=0, t) = A_o, \quad (5)$$

where the position $x=0$ is defined such that the filament shows the maximum radius after being extruded from the die due to the Barus effect.²³ In addition, the normal stress difference σ in eq.(3) is zero at $x=0$ because the polymer chains at $x=0$ are fully relaxed and isotropic, as given by assumption (ii). In the spinning process, a tension is imparted to the polymer melt filament extruded from the die by being taken up at the winding section at high speeds. The filament is extended and becomes slender in the air gap region between the exit of the die and the water bath, and then it is cooled down by going

into a cool medium, the water bath. As mentioned in assumption (v), because the filament is solidified just after entering the water bath (see Fig.1), the velocity of the filament at $x=L$ is the same as the winding velocity, V_w . Namely, the boundary condition for V at $x=L$ is given as

$$V(x=L, t) = V_w. \quad (6)$$

The velocity ratio between V_o and the winding velocity V_w is called the draw ratio, $Dr \equiv V_w/V_o$. It is known that such elongational flow becomes unstable above a critical draw ratio $Dr^{(c)}$, where the draw resonance phenomenon appears and the cross section area of the fiber varies periodically. In addition, the air-gap distance, temperature and viscoelastic properties of the polymer melt also affect the stability of the spinning process and the material properties of the resultant fibers.^{1,2}

All the variables defined at the macroscopic level are scaled by using the spatial unit $\ell^{(M)}=L$, time unit $t_o^{(M)}(=L/V_o)$ and stress unit $\sigma_o^{(M)}$. The symbols with the superscript "(M)" stands for various units used at the Macroscopic level, and in the next subsection the symbols with the superscript "(m)" are used for units used at the microscopic level. In addition, the cross section A is scaled by A_o . The stress unit $\sigma_o^{(M)}$ will be explained in detail in the next subsection, after we introduce the corresponding constitutive equation. All scaled variables are expressed with a tilde symbol on top, as $\tilde{V}=V/V_o$, $\tilde{A}=A/A_o$, $\tilde{\sigma}=\sigma/\sigma_o^{(M)}$, $\tilde{F}=F/A_o\sigma_o^{(M)}$, $\tilde{x}=x/\ell_o^{(M)}$ and $\tilde{t}=t/t_o^{(M)}$. After scaling, equations (1)-(4) are found to be:

$$\frac{\partial \tilde{A}(\tilde{x}, \tilde{t})}{\partial \tilde{t}} = -\frac{\partial}{\partial \tilde{x}} \left(\tilde{A}(\tilde{x}, \tilde{t}) \tilde{V}(\tilde{x}, \tilde{t}) \right), \quad (7)$$

$$\tilde{F}(\tilde{x}, \tilde{t}) = \tilde{A}(\tilde{x}, \tilde{t}) \tilde{\sigma}(\tilde{x}, \tilde{t}), \quad (8)$$

$$\tilde{\sigma}(\tilde{x}, \tilde{t}) = \tilde{\sigma}_{xx} - (\tilde{\sigma}_{yy} + \tilde{\sigma}_{zz})/2. \quad (9)$$

$$\text{Re} \tilde{A} \left(\frac{\partial \tilde{V}}{\partial \tilde{t}} + \tilde{V} \frac{\partial \tilde{V}}{\partial \tilde{x}} \right) = \frac{\partial \tilde{F}}{\partial \tilde{x}} \quad (10)$$

where $\text{Re} = \rho V_o^2 / \sigma_o^{(M)}$ is the Reynolds number. The boundary conditions are given as

$$\tilde{V}(0, \tilde{t}) = 1, \quad \tilde{V}(1, \tilde{t}) = Dr \quad \text{and} \quad \tilde{A}(0, \tilde{t}) = 1. \quad (11)$$

As seen from the set of equations (7)-(10) and the boundary conditions (11), the control parameters at the macroscopic level are the draw ratio Dr and the Reynolds number Re .

In industrial applications, the velocity of the spinning fiber is roughly categorized into four regions^{1,16}: (i) a low speed region ($\lesssim 2000\text{m/min}$), (ii) a partially oriented yarn region ($\sim 3500\text{m/min}$), (iii) a high speed region ($\sim 6000\text{m/min}$) and (iv) an ultra-high speed region ($>6000\text{ m/min}$). The length of the air gap and the diameter of the nozzle are $0.05\text{m} \lesssim L_o \lesssim 0.1\text{m}$ (standard value $\sim 0.05\text{m}$) and $A_o \approx 0.2\text{mm}$, respectively. If one considers a melt spinning process with a spinning velocity V_w higher than that in the low speed region ($\lesssim 2000\text{m/min}$), and uses $\eta_s = 10^2 \text{ Pa} \cdot \text{s}$ as a typical value for the shear viscosity¹⁶ of the polymer melt used in the spinning, along with a density $\rho_o = 10^3 \text{ kg/m}^3$, air gap $L_o = 0.05\text{m}$ and a typical stress of $\sigma_o^{(M)} (= \eta_s V_o / L_o)$, the Reynolds number Re

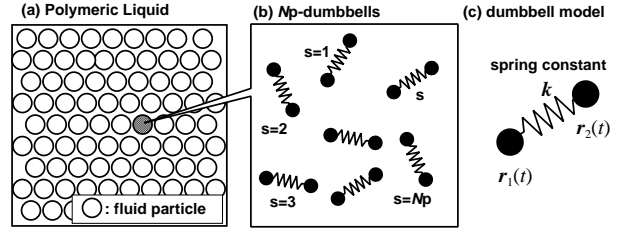


Fig. 2. Schematic views of (a) fluid particles composing a polymeric liquid, (b) N_p -dumbbells in a fluid element and (c) the dumbbell model.

is found to be in the regime $\text{Re} \gtrsim 16.7/Dr$, where the velocity of the fiber at the exit of the die is estimated as $V_o = V_w/Dr$. In the following sections, we separately investigate the two Reynolds number regimes (a) $\text{Re} \rightarrow 0$ and (b) finite Re , for draw down ratios in the range $10 \leq Dr \leq 30$.

2.2 Microscopic model for the polymer chains and stress tensor

The rheological properties of the polymeric fluid play an essential role in determining the stability of the spinning process. Usually, a constitutive equation is used to theoretically predict the flow behavior. Until now, numerous constitutive equations have been proposed, and each of them presents its own advantages and disadvantages. The main problems of using such a constitutive equation approach are: (a) how to choose a proper constitutive equation, which is able to predict the rheological properties of a target polymeric liquid, and (b) the difficulty in connecting the stress evaluated by the constitutive equation to the microscopic state of the polymer chains. In the present work, instead of using a macroscopic constitutive equation, we employ a microscopic model to describe the rheology of the fluid, where the stress tensor is evaluated in a statistical manner by considering the microscopic states of the polymer chains. So far, many microscopic polymer models have been proposed, such as the Rouse model,²² the simple and finite extensible Hookean-dumbbell models,²³ the Kremer-Grest-beads-spring model,²⁴ the Doi-Edwards reptation model,²⁵ the primitive chain network model,²⁶ and the slip-link models,²⁷⁻³¹ and so on, and they have all been used to investigate the bulk rheological properties of polymeric fluids. Here we employ the simple Hookean dumbbell model as a microscopic model in our multiscale simulation of the melt spinning process. The reasons why we have selected this particular model are the following:

- (i) In the limit when the number of Hookean dumbbells goes to infinity, the corresponding constitutive equation is known. This allows us to assess the accuracy of our multiscale simulation.
- (ii) The computational cost is significantly lower than the other microscopic polymer models.

The Hookean dumbbell is composed of two beads connected by a spring with a spring constant k . We consider that a fluid

particle with a volume v_o in a fluid contains N_p -dumbbells as shown in Fig.2(a) and (b). It is assumed that no interaction does work among different dumbbells. The equation for the relative vector \mathbf{r} between two beads is given as²³

$$\frac{d\mathbf{r}}{dt} = \boldsymbol{\kappa} \cdot \mathbf{r} - \frac{2}{\zeta} k\mathbf{r} + \frac{1}{\zeta} \mathbf{R} \quad (12)$$

where ζ is the frictional coefficient, $\boldsymbol{\kappa}$ is the velocity gradient tensor which is defined by $\kappa_{\alpha\beta} = \partial V_\alpha / \partial x_\beta$ ($\alpha, \beta \in \{x, y, z\}$) and \mathbf{R} is a random force which satisfies the fluctuation-dissipation theorem. Using the obtained relative vectors \mathbf{r} from eq.(12) and the spring forces \mathbf{F} for all the dumbbells, the stress tensor in a fluid particle can be evaluated by the following statistical average over constituent dumbbells,²³ which is known as Kramers' relation:

$$\sigma_{\alpha\beta} = -\frac{N_p}{v_o} \langle r_\alpha F_\beta \rangle \simeq -\frac{n}{N_p} \sum_{s=1}^{N_p} r_\alpha^{(s)} F_\beta^{(s)}, \quad (13)$$

where $\langle \dots \rangle$ denotes the statistical average of (\dots) and can be evaluated approximately by the average over N_p -dumbbells, the variables with the upperscript (s) mean the ones of the s -th dumbbell, N_p is the number of dumbbells in the system of volume v_o and $n \equiv N_p / v_o$ is the number density of dumbbells. Using the expression of the spring force $\mathbf{F} = -k\mathbf{r}$, the stress tensor is microscopically expressed as

$$\sigma_{\alpha\beta} = n \left(k \langle r_\alpha r_\beta \rangle - k_B T \delta_{\alpha\beta} \right) \quad (14)$$

where k_B is the Boltzmann constant, T the temperature, and σ is redefined by subtracting a constant diagonal tensor from it, such that it is equivalent to the zero tensor in the quiescent state, by using the following relation $\langle r_\alpha r_\beta \rangle_{\text{eq}} = k_B T \delta_{\alpha\beta} / k$. Using eq.(14), the constitutive equation of the stress defined by (14), can be derived to be

$$\frac{d\sigma_{\alpha\beta}}{dt} = \kappa_{\alpha\gamma} \sigma_{\gamma\beta} + \sigma_{\alpha\gamma} \kappa_{\beta\gamma} + n k_B T (\kappa_{\alpha\beta} + \kappa_{\beta\alpha}) - \frac{4k}{\zeta} \sigma_{\alpha\beta}, \quad (15)$$

where the repeated indices are summed over $\{x, y, z\}$. Equation (15) is referred to as the upper convected Maxwell constitutive equation. It should be noted that in the limit $N_p \rightarrow \infty$, the stress evaluated by eq.(14) converges to that evaluated by eq.(15). Because N_p is always finite in a realistic numerical simulations, the influence on rheological properties of the statistical error always remains, depending on how large N_p is, as shown in the last paragraph of this section.

When constructing dimensionless expressions for eqs.(12)-(15) the Deborah number naturally appears. The Deborah number De is the ratio of an apparent convective time $t_o^{(M)} (= L / V_o)$ of a material point in the air gap region and the relaxation time of the dumbbell λ ($\equiv \zeta / (4k)$), and is defined as $\text{De} = \lambda / t_o^{(M)}$. To obtain dimensionless expressions for eqs.(12)-(15), $t_o^{(m)}$, $\ell_o^{(m)}$ and $\sigma_o^{(m)}$ are used as units of time, length and stress, respectively. We set the units at the microscopic level to be the same as those at the macroscopic level, except that the length of dumbbell is scaled by the equilibrium length of a dumbbell $\ell_{\text{eq}} = \sqrt{3k_B T / k}$. Namely, we chose as units of

length and time $\ell_o^{(m)} = \ell_o^{(M)} = L_o$ and $(t_o^{(m)} = t_o^{(M)} = L / V_o)$, respectively. We now introduce the unit of stress, which we did not clearly explain when introducing the macroscopic level model in eqs.(8)-(9), since the constitutive equation had not yet appeared at that time. We define the units of stress as $\sigma_o^{(m)} = \sigma_o^{(M)} = n k_B T \lambda / t_o$. It should be noted $\sigma_o^{(m)}$ can also be expressed as $\sigma_o^{(m)} = \eta_s V_o / L_o$, with η_s being the shear viscosity of Maxwell fluid, given by $n k_B T \lambda$. Hereafter t_o ($\equiv t_o^{(m)} = t_o^{(M)}$) and σ_o ($\equiv \sigma_o^{(m)} = \sigma_o^{(M)}$) will be used as units of time and stress. Using the units defined above, eqs.(12)-(15) are rescaled and found to be

$$\frac{d\tilde{\mathbf{r}}(\tilde{t})}{d\tilde{t}} = \tilde{\boldsymbol{\kappa}} \cdot \tilde{\mathbf{r}}(\tilde{t}) - \frac{1}{2\text{De}} \tilde{\mathbf{r}}(\tilde{t}) + \sqrt{\frac{1}{3\text{De}}} \tilde{\mathbf{R}}(\tilde{t}). \quad (16)$$

where $\tilde{\boldsymbol{\kappa}} = \boldsymbol{\kappa} t_o$, $\tilde{\mathbf{R}}$ is defined by $\tilde{\mathbf{R}} = \sqrt{t_o / 4k_B T \zeta} \mathbf{R}$ and satisfies $\langle \tilde{\mathbf{R}}_\alpha \rangle = 0$ and $\langle \tilde{\mathbf{R}}_\alpha(\tilde{t}) \tilde{\mathbf{R}}_\beta(\tilde{t}') \rangle = \delta_{\alpha\beta} \delta(\tilde{t} - \tilde{t}')$. The dimensionless expression for the stress tensor is given as

$$\tilde{\sigma}_{\alpha\beta} = \frac{3}{\text{De}} \left(\langle \tilde{r}_\alpha \tilde{r}_\beta \rangle - \frac{1}{3} \delta_{\alpha\beta} \right). \quad (17)$$

The dimensionless expression of eq.(15) is found to be

$$\frac{D\tilde{\sigma}_{\alpha\beta}}{D\tilde{t}} = \tilde{\kappa}_{\alpha\gamma} \tilde{\sigma}_{\gamma\beta} + \tilde{\sigma}_{\alpha\gamma} \tilde{\kappa}_{\beta\gamma} + \frac{1}{\text{De}} (\tilde{\kappa}_{\alpha\beta} + \tilde{\kappa}_{\beta\alpha}) - \frac{1}{\text{De}} \tilde{\sigma}_{\alpha\beta}. \quad (18)$$

Unless otherwise stated, in what follows we omit the tilde symbols on dimensionless variables, except where it might cause confusion to occur, in order to simplify the resulting expressions. As seen from the dimensionless equations (16)-(18), De is the only control parameter in the equations at the microscopic level. Therefore, the control parameters in the present system are the draw ratio Dr , the Reynolds number Re and the Deborah number De .

As mentioned in the previous paragraph, the statistical error of the stress tensor depends on the number of dumbbells N_p used in the simulation. Here we show how the stress evaluated by a microscopic system consisting of a finite number of N_p deviates from the stress calculated by the mathematically equivalent constitutive equation (15), which will give us useful information on how large N_p should be in order to obtain reasonable results when using multiscale simulations to describe melt spinning processes. In Fig.3, we show the time evolution of the stresses in a uniaxial elongational start-up flow with a constant velocity gradient $\kappa_{xx} = 25$ ($\kappa_{yy} = \kappa_{zz} = -\kappa_{xx}/2$, $\kappa_{\alpha\beta} = 0$ for $\alpha \neq \beta$) for three different number of dumbbells, $N_p = 10^3$, 10^4 and 10^5 , with a Deborah number $\text{De} = 10^{-2}$. The value $\kappa_{xx} = 25$ is chosen as a typical velocity gradient used in our multiscale simulations and $\text{De} = 10^{-2}$ is chosen so that the fluid shows a viscoelastic behavior over a time period t^* , during which a material point runs through the air gap region. The time period t^* is roughly estimated to be $0.3t_o$ by using $\text{Dr} \approx \kappa_{xx} = 25$ and the expression $t^* = (\text{Dr} - 1) / (\text{Dr} \ln \text{Dr})$ for the Newtonian fluid.⁵² As shown in Fig.3, the deviation of the stress σ_{xx} and σ_{yy} from the theoretical lines obtained by using the upper convected Maxwell equation (15) decreases with increasing N_p . We confirmed that the standard deviation from $\sigma_{\alpha\alpha}^{(M)}$ decreases proportional

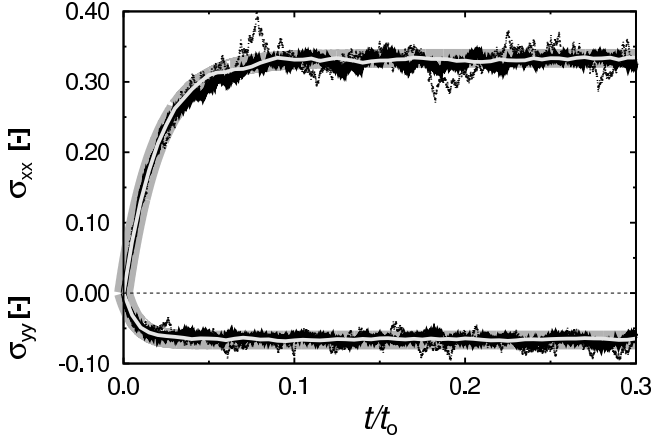


Fig. 3. Time evolutions of σ_{xx} and σ_{yy} in a start-up flow under a constant uniaxial elongational flow ($\kappa_{xx}=25$) for Maxwell fluids ($De=10^{-2}$) consisting of non-interacting N_p -dumbbells ($N_p=10^3$ (dotted-line), 10^4 (black solid-line) and 10^5 (white solid-line)). The very thick grey line stands for the theoretical lines obtained by the corresponding constitutive equation (15).

to $1/\sqrt{N_p}$. Judging from Fig.3 and from the view point of the trade-off between the accuracy of the stress and the computational cost, we decided to use $N_p=10^4$ as the number of dumbbells on a single Lagrangian particle (*i.e.*, on each microscopic simulator) in the multiscale simulations presented in the next section.

2.3 Multiscale simulation method

We performed numerical simulations of a spinning process in a multiscale way, where a set of macroscopic equations are solved by communicating with an ensemble of embedded microscopic simulation systems. The fluid in the spinning process is assumed to be a viscoelastic fluid described by a set of non-interacting Hookean dumbbells defined in eq.(12), which is equivalent to a Maxwell viscoelastic fluid, described by eq.(15). Because the stress of a viscoelastic fluid depends on the history of the strain and/or strain-rate that the microscopic molecules have experienced in the past, it is suitable to evaluate the stress tensor on a fluid particle based on the Lagrangian picture (see Fig.4). As shown in Fig.4(b), the spinning line in the air gap region is divided by $(M+1)$ -grid points, in other words, the line is divided into M regions with a constant spatial interval $\Delta x=1/M$, to solve the equations at the macroscopic level in the Eulerian fashion. On a grid point i ($0 \leq i \leq M$), the variables $A_i(t)$ and $V_i(t)$ are defined ($A_i(t) \equiv A(i\Delta x, t)$ and $V_i(t) \equiv V(i\Delta x, t)$), on the other hand, the stress $\sigma_I(t)$ is defined on a staggered lattice point $I \equiv i - 1/2$, ($\sigma_I(t) \equiv \sigma(I\Delta x, t)$). In addition, N_L -Lagrangian fluid particles are distributed on the spinning line, on each of which a microscopic simulation system is embedded. The stress tensor on a staggered lattice point I is evaluated by an average over the stress tensors of all the Lagrangian particles located within the spatial interval $[(i-1)\Delta x, i\Delta x]$.

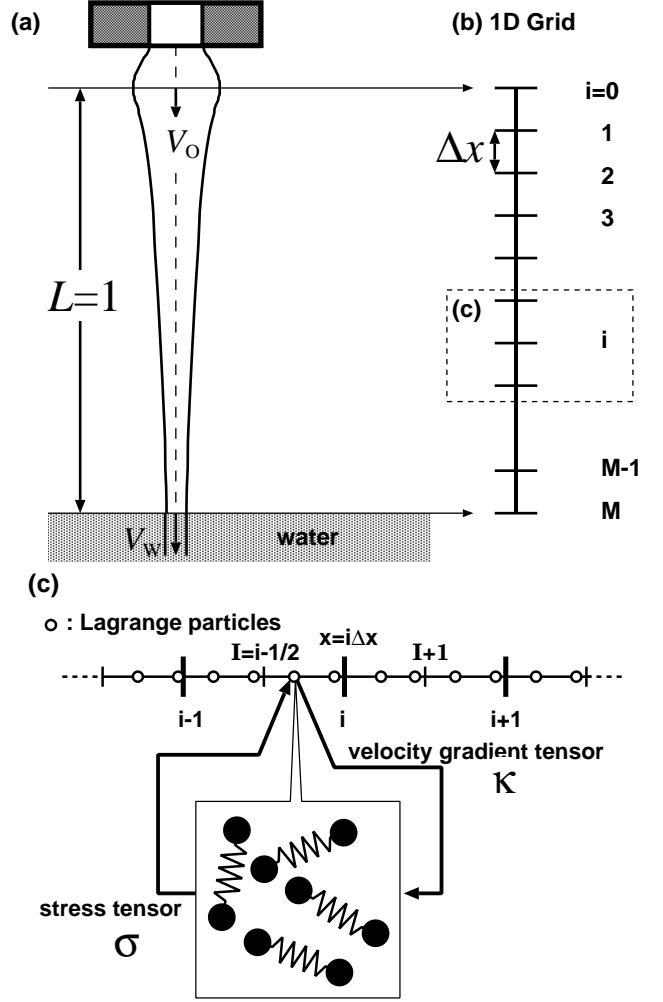


Fig. 4. Schematic views of (a) the filament in melt spinning process, (b) the grid used in solving the macroscopic equations, and (c) the Lagrange fluid particles denoted by open circles on the spinning line.

(i) Cross section area update

Suppose that the values of A_i and V_i at a time t are known. The cross section area $A_i(t)$ at a lattice point i ($1 \leq i \leq M$) (see Fig.4(b)) is updated by the following discretized form of equation of eq.(7)

$$A_i(t + \Delta t) = A_i(t) + \delta A_i \quad (19)$$

where δA_i is defined at time t as

$$\delta A_i = -(A_{i+1}V_{i+1} - A_{i-1}V_{i-1})\Delta t/2\Delta x \quad \text{for } 1 \leq i < M \quad (20)$$

and $\delta A_M = -(3A_MV_M - 4A_{M-1}V_{M-1} + A_{M-2}V_{M-2})\Delta t/2\Delta x$ with the boundary conditions $A_0(t) = 1$ and $V_0(t) = 1$ in eq.(11).

(ii) Velocity field update

The velocity $V_i(t + \Delta t)$ is evaluated from eq.(10). As we estimated at the end of Sec. 2.2, for moderate spinning the Reynolds number is in the range $Re \gtrsim 0.1$, but Re may become very small when we perform a very slow spinning or use a polymeric fluid with a very high viscosity. Because the ap-

appropriate numerical scheme for evaluating $V_i(t + \Delta t)$ depends on Re , we separately explain the schemes used to update $V_i(t)$ for two cases, (a) $\text{Re} \rightarrow 0$ and (b) finite Re .

(a) $\text{Re} \rightarrow 0$

For a very low Reynolds number, the force balance equation $\partial F / \partial x = 0$ will be satisfied instantaneously. Namely, at every single time step, the tension $F(I)$ must be balanced throughout the system. In the numerical simulation, the following condition should be satisfied:

$$\frac{\delta F}{F_{\text{ave}}} \equiv \frac{|\text{Max}\{F(I)\} - \text{Min}\{F(I)\}|}{F_{\text{ave}}} < \epsilon \quad (21)$$

where $\text{Max}\{F(I)\}$, $\text{Min}\{F(I)\}$ and F_{ave} denote the maximum, minimum and average of $F(I)$, respectively, and ϵ is a suitably small value which sets the tolerance level. To find the velocity $V_i(t + \Delta t)$ that satisfies condition (21), a relaxation method or a quasi-Newtonian method can be used. In a simple relaxation method, the trial velocity $V_i^{(n)}$ at $t + \Delta t$ is repeatedly updated by using the following equation

$$V_i^{(n+1)} = V_i^{(n)} + \frac{\delta}{\Delta x} [F^{(n)}(I + 1) - F^{(n)}(I)] \quad (22)$$

until the force balance condition given in eq.(21), with the updated stress values $\sigma_I^{(n+1)}(t + \Delta t)$ obtained from the velocity gradient field corresponding to $V_i^{(n+1)}$, is satisfied. In eq.(22), δ is a small virtual time increment, n is the internal counter for the iteration step at $t + \Delta t$, $F^{(n)}(I) \equiv \sigma_I^{(n)}(t + \Delta t)A_I(t + \Delta t)$ and $A_I \equiv (A_{i-1} + A_i)/2$. This means that at each step of the iterative procedure used to find the $V_i(t + \Delta t)$ satisfying the force balance condition, the stress tensor σ_I must be recalculated according to the velocity gradient tensor corresponding to the trial $V_i^{(n)}$. As an alternative to this simple iterative procedure, the Broyden method is one of the quasi-Newtonian methods used to find the roots of multi-dimensional non-linear equations. This method can be very efficient, provided one gives an appropriate initial guess for $\{V_i(t + \Delta t)\}$, but if not, it can take many steps, or worse, it is possible that it never converges. Generally speaking, the relaxation method requires much more computational time than the Broyden method, but is relatively less-sensitive to the initial guess for V_i , although a better initial guess will result in faster convergence. However, for our present application, both methods required many internal iteration steps at each time step, and the velocity field sometimes would not converge within the specified threshold for the number of iteration steps, above which a simulation would not finish within a realistic time. As will be shown in Sec.3(a), we chose the Broyden method to evaluate the velocity field because it was relatively faster than the simple relaxation method.

(b) Finite Re

As estimated before, for relatively high speed spinning ($\geq 2000\text{m/s}$), the Reynolds number is in the range $\text{Re} \geq 16.7/\text{Dr}$ (e.g., 0.56 for $\text{Dr}=30$). In such situations, the contributions from the inertial term in eq.(10) cannot be ignored. Therefore, we directly evaluate the velocity $V_i(t + \Delta t)$

by applying an explicit scheme for the momentum equation (10) as

$$V_i(t + \Delta t) = V_i(t) - (V_{i+1}(t))^2 - (V_{i-1}(t))^2 \Delta t / (4\Delta x) + \text{Re}^{-1}(\Delta t / \Delta x) [\sigma_{I+1}A_{I+1} - \sigma_I A_I] / A_i. \quad (23)$$

(iii) Lagrange particle update

After obtaining the velocity V_i on the Eulerian grids, as described above in the calculation step (ii), the velocities and velocity gradient tensors at all the positions of the Lagrange particles are evaluated by interpolating the V_i . As an interpolating function for the velocity and velocity gradient tensor $\kappa_{\alpha\beta}$ we use a quadratic and linear function, respectively. Then, all the fluid particles are advected according to the local velocities evaluated at their positions. When the position $X(t)$ of a Lagrange particle closest to $x=0$ becomes larger than ΔX_{init} , a new Lagrangian particle is inserted into the system at position $X' (= X - \Delta X_{\text{init}})$, in such a way that the initial distance between two adjacent Lagrange particles is set to a constant ΔX_{init} . Since the time interval Δt used in our simulations is small, the initial position X' of the newly inserted Lagrangian particle is almost zero. In the simulations which will be shown in the next section, the initial distance ΔX_{init} is set to $\Delta X_{\text{init}} \approx 10^{-4}$ in (a), and $X_{\text{init}} = 10^{-4}$ for $\text{Dr}=10, 20$ and 0.5×10^{-4} for $\text{Dr}=30$ in (b). The dumbbells on the newly inserted particle are set so as to satisfy the relation $\langle r_\alpha r_\beta \rangle = \delta_{\alpha\beta}/3$, which results in a zero stress tensor.

(iv) Bridge between macro- and microscopic simulators

A microscopic system embedded in a fluid particle is used to obtain a local stress tensor as a response to the velocity gradient tensor at the position of a particle on the spinning line. The resulting stress tensors on the particles are transferred to the macroscopic system as stress tensors at the corresponding positions, then, the stress tensor σ_I on the staggered lattice I is evaluated as an average over the stresses on the particles located in the region- I (i.e., the spatial interval $[(i-1)\Delta\bar{x}, i\Delta\bar{x}]$). Generally speaking, the step to evaluate the stress tensor on each Lagrangian particle demands a tremendous computational expense, because of the large number of molecular agents (dumbbells) present in a single Lagrangian particle. Therefore, we have implemented a parallel computational code by using MPI (Message Passing Interface), specifically designed for the calculation of the stresses, which plays an essential role in reducing the computational time to a realistic value. The number of cores used in the parallel computations is ranged from 64 to 96 in (a), is 24 in (b).⁵³ In this way, we have performed the communication between macro- and microscopic systems.

3. Results of the Multiscale simulations

In the multiscale simulations, we used $M=100$ as the number of the grid points, with $N_p=10^4$ in each microscopic system of Lagrangian material points, as explained in the previous section. In the following, we present the results obtained in the typical cases of (a) $\text{Re} \rightarrow 0$ and (b) finite Re . The ini-

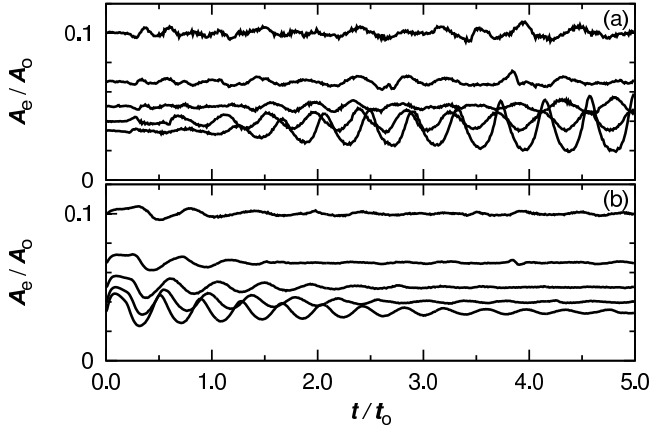


Fig. 5. Time evolution of the cross section area A_e at an end point ($x=1$) for $Dr=10, 15, 20, 25, 30$ (from top to bottom) at (a) $De=10^{-3}$ and (b) $De=10^{-2}$.

tial configurations of the dumbbells in each of the Lagrangian particles in (a) and (b) are set to be those at the relaxed state, *i.e.*, so as to give $\langle r_\alpha r_\beta \rangle = \delta_{\alpha\beta}/3$. The initial values of the cross section area and velocity along the spinning line are those of the analytic solution for a Newtonian fluid at the specified Dr . (a) $Re \rightarrow 0$

In the limit $Re \rightarrow 0$, the tension will be balanced within an infinitely small time duration, therefore, the velocity field must be determined so as to satisfy $\partial F / \partial x = 0$. To obtain a velocity field which satisfies this constraint, we used the Broyden method mentioned in the previous section. All the simulations in (a), the time increment Δt is set to 10^{-4} . Fig.5 shows the time evolutions of the cross section area $A_e \equiv A(x=1, t)$ at the end of air gap region for $Dr=10, 15, 20, 25, 30$ (from top to bottom) at (a) $De=10^{-3}$ and (b) $De=10^{-2}$. In the case of (a) $De=10^{-3}$, the draw resonance phenomenon takes place at $Dr \gtrsim 20$. In the case of (b) $De=10^{-2}$, although large oscillations of $A_e(t)$ are observed at the beginning, which increase with increasing values of Dr , these oscillations are finally suppressed after $t \approx 4$. Namely, no periodic change in the cross section area could be observed in (b), although a fluctuation of $A_e(t)$ still exists at long times. Note that in the Newtonian fluid, the critical draw ratio above which the draw resonance takes place is $(Dr)_c=20.21$.^{8,12} It seems that $A_e(t)$ for $Dr=20$ and $De=10^{-3}$ starts to show a periodic change. This result might be attributed to the effect of noise coming from the finite number of dumbbells we have used, but further investigations should be performed in order to clarify such noise and finite-number effects. It is considered that the suppression of the draw resonance in case (b) $De=10^{-2}$ originates from the elastic effect of the dumbbells.

Fig.6 shows the spatial distribution of Lagrangian particles existing in the region $[x, x + \Delta x]$ with $\Delta x=1/M$, at $t=5$, for $Dr=10, 15$ and 20 in $De=10^{-3}$ (grey) and 10^{-2} (white). The lower and higher histograms, respectively, denote the data for $Dr=10$ and 20 , and the results for $Dr=15$ are drawn using filled circles for $De=10^{-3}$, and open circles for $De=10^{-2}$. When the position of the closest Lagrangian particle to $x=0$ becomes

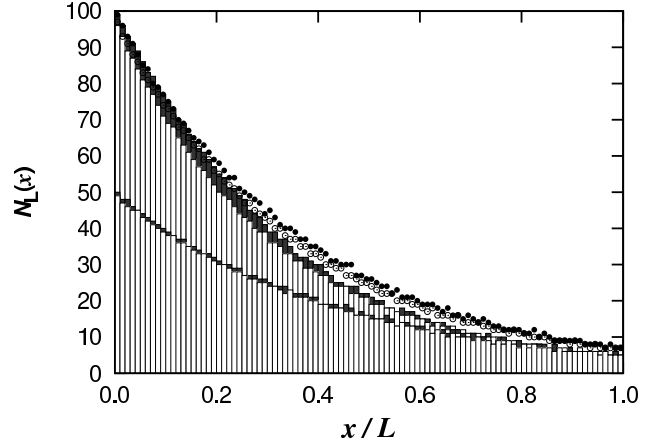


Fig. 6. Spatial distributions of the number of Lagrangian particles $N_L(x)$ existing in the interval $[x, x + \Delta x]$ on the spinning line for $De=10^{-3}$ (grey) and $De=10^{-2}$ (white) at $t=5$ in $Dr=10, 15$ and 20 . The lower and higher histograms stand for $Dr=10$ and 20 , respectively, but the results for $Dr=15$ are drawn using filled circles ($De=10^{-3}$) and open circles $De=10^{-2}$, to easily distinguish them from the other cases.

larger than a certain threshold value $\Delta X_{init}(=10^{-4})$, a new Lagrangian particle is inserted at a new position ($X \approx 0$), in such a way that the initial distance between the adjacent particles is constant ΔX_{init} . Hence, the distribution of Lagrangian particles shows almost no change when the velocity field has reached a steady state. It should be noted that even when a draw resonance takes place, the change in the velocity field is not so large that the particle distribution is significantly altered. The total numbers of Lagrangian particles $N_L^{(Total)}$ for $Dr=10, 15$ and 20 at $t=5$ are $N_L^{(Total)} \approx 1900, 3300$ and 3000 , respectively, and these numbers are almost constant for $t \gtrsim 4$. To suppress the statistical error in evaluating the stress, it is important to have a large enough number of Lagrangian particles, especially in the regions close to $x=1$, because the density of particle becomes smallest at this position. For all the cases considered here, we choose an appropriately small ΔX_{init} so that the number of particles at $x \approx 1$ is roughly constant, which is enough to suppress the statistical error below a certain level. Although a smaller ΔX_{init} is better for suppressing the error, a larger number of total Lagrangian particles will make the computational cost increase significantly.

Fig.7 shows the velocity profiles on the spinning line at $t=5$ for the six combinations of $Dr=10, 15, 20$ and $De=10^{-3}, 10^{-2}$. For both $De=10^{-2}$ and 10^{-3} , the velocities for $Dr=10$ and 15 coincide with the corresponding ones of a Newtonian fluid (solid line) given by eq.(A-4) in Appendix, although a small deviation from the solid line can be seen in the case of $De=10^{-2}$ and $Dr=15$. We can infer from these results that the dumbbells in these cases are stretched, which will be confirmed later in Fig.10. At $Dr=20$, the velocity profiles for $De=10^{-3}$ mostly coincide with the Newtonian fluid results, but the one for $De=10^{-2}$ shows a clear deviation towards larger values. This is because of the elastic effect coming from the slow relaxation of stretched dumbbells, as seen from the

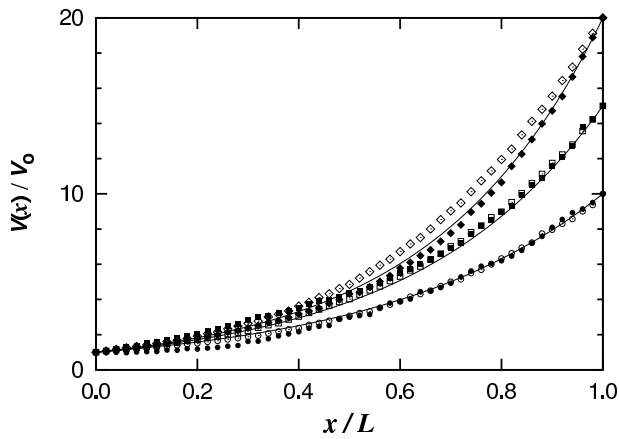


Fig. 7. Velocity profiles at $t=5$ for $Dr=10$ (circle), 15 (square) and 20 (diamond) on the spinning line obtained by the MSS method for $De=10^{-3}$ (filled symbol) and 10^{-2} (open symbol). The lines stand for the velocity profiles of Newtonian fluids for $Dr=10$, 15 and 20, from bottom to top, respectively.

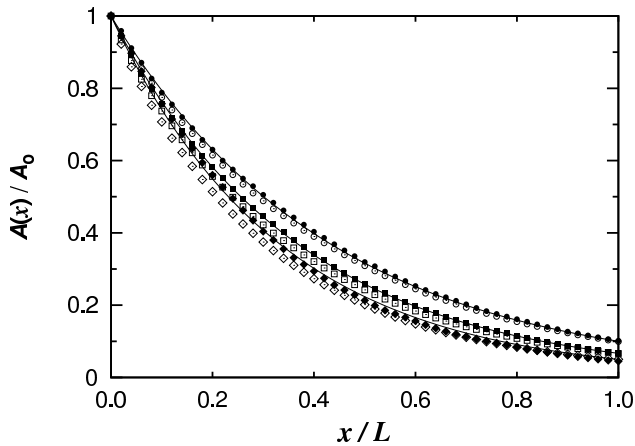


Fig. 8. Cross section area $A(x)$ of the fiber obtained by the MSS method for $Dr=10$ (circle), 15 (square) and 20 (diamond), and $De=10^{-3}$ (filled symbols) and 10^{-2} (open symbols). The solid lines are the cross section areas for a corresponding Newtonian fluid for $Dr=10$, 15 and 20, from top to bottom, respectively.

analytic solution (eq.(A-5) in Appendix) in the elastic limit, where $V(x)$ becomes a linear function of x . In Fig.8, we plot the cross section area along the spinning line for $Dr=10$, 15 and 20 at $De=10^{-3}$ and 10^{-2} . The cross section areas at $De=10^{-3}$ correspond almost exactly to the analytic solution for the Newtonian fluid. For the $De=10^{-2}$ cases, on the other hand, the lines deviate towards smaller (thinner) values, with respect to the corresponding Newtonian solution (eq.(A-4) in Appendix). This tendency for A is consistent with what would be expected given the velocity profiles shown in Fig.7. We can see that the A_e are mainly determined by Dr , but they do not depend strongly on De . The state of the dumbbells at $x \approx 1$ for different De , but for the same Dr , however, are significantly different to each other, as can be clearly seen in Fig.10.

As mentioned in the previous section, the tension along the

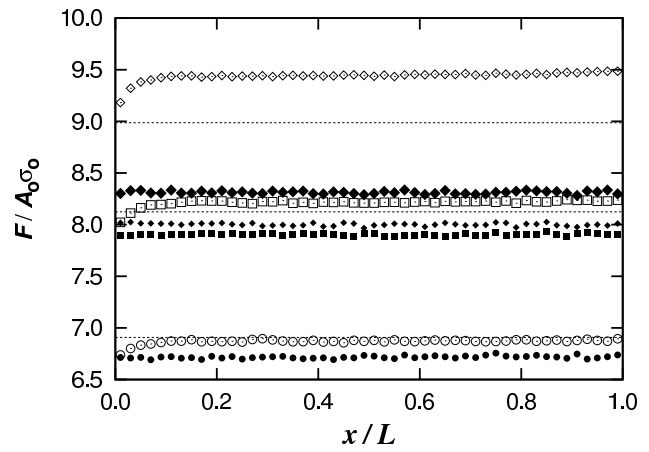


Fig. 9. Tensions F on the spinning line at $t=5$ for $Dr=10$ (circle), 15 (square) and 20 (diamond), and $De=10^{-3}$ (filled symbols) and 10^{-2} (open symbols). As a reference, the tension at $t=3$ for $Dr=20$ and $De=10^{-3}$ is also shown by larger filled diamonds. The dotted lines stand for tensions of a Newtonian fluid, $F=3 \ln(Dr)$ (See eq.(A-4) in Appendix), for $Dr=10$, 15 and 20 from bottom to top, respectively.

Table I. Maximum (F_{\max}), minimum (F_{\min}), average (F_{ave}) and relative errors ($\delta F/F_{\text{ave}}$) of the fiber tension $F(x)$ at $t=5$ for (a) $Dr=10$ (b) $Dr=15$ (c) $Dr=20$ (d) $Dr=25$ (e) $Dr=30$ at two typical Deborah numbers ($De=10^{-3}$ and 10^{-2}), where $\delta F = F_{\max} - F_{\min}$.

Dr	De	F_{\max}	F_{\min}	F_{ave}	$\delta F/F_{\text{ave}}$
(a) 10	10^{-3}	2.25×10^{-3}	2.23×10^{-3}	2.24×10^{-3}	1.05%
	10^{-2}	2.32×10^{-2}	2.27×10^{-2}	2.39×10^{-2}	2.65%
(b) 15	10^{-3}	2.26×10^{-3}	2.26×10^{-3}	2.63×10^{-3}	0.58%
	10^{-2}	2.79×10^{-2}	2.70×10^{-2}	2.74×10^{-2}	3.02%
(c) 20	10^{-3}	2.27×10^{-3}	2.27×10^{-3}	2.67×10^{-3}	0.73%
	10^{-2}	3.21×10^{-1}	3.11×10^{-2}	3.15×10^{-2}	3.18%
(d) 25	10^{-3}	3.34×10^{-3}	3.31×10^{-3}	3.32×10^{-3}	0.89%
	10^{-2}	3.60×10^{-2}	3.47×10^{-2}	3.53×10^{-2}	3.83%
(e) 30	10^{-3}	4.52×10^{-3}	4.45×10^{-3}	4.50×10^{-3}	1.70%
	10^{-2}	3.92×10^{-1}	3.76×10^{-2}	3.84×10^{-2}	4.23%

fiber must be balanced. In our numerical simulations, this condition is relaxed by introducing a tolerance ϵ , as explained in eq.(21), which we have set to $\epsilon=0.05$. In Fig.9, the fiber tension along the spinning line is plotted, and we can clearly see that the tension is almost perfectly balanced. In addition, to understand to what extent the tension balance holds under the various conditions in our simulations, we present the maximum, minimum, and average tension at $t=5$ along the spinning line, as well as the relative deviation of the tension from its average value in Table I. As seen from the table, the relative errors are maintained at less than 5%, as the tolerance ϵ in eq.(21) is set to 0.05. As seen from Fig.9, for a given

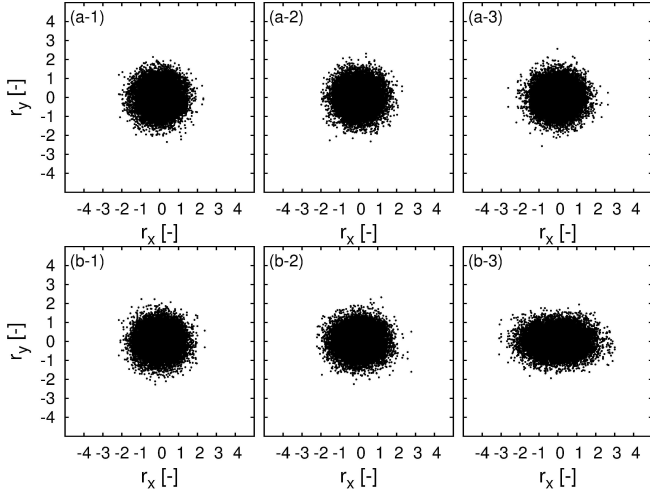


Fig. 10. Distribution of the connecting vectors for $Dr=15$ in a fluid particle at (1) $x \approx 0.1$, (2) $x \approx 0.5$ and (3) $x \approx 1$ at $t=5$ for (a) $De=10^{-3}$ and (b) $De=10^{-2}$.

Dr , the tension at $De=10^{-2}$ (open symbols) is higher than the one at $De=10^{-3}$ (corresponding filled symbols). Although it is expected that the tension at $De=10^{-3}$ (see filled symbols in Fig.9) should be closer to the Newtonian values (shown as dashed lines), the tension at $t=5$ for $De=10^{-2}$ is actually closer. Particularly, the tension at $De=10^{-3}$ for $Dr=20$ is considerably smaller than that of the corresponding Newtonian fluid (see F in eq.(A.4)). We confirmed that the tension is changing largely with time depending on A_e in Fig.5. This is a reason why the tension at $t=5$ became smaller than that of the Newtonian fluid. As a reference, the tension at $t=3$ for $De=10^{-3}$ and $Dr=20$ is also shown in Fig.9, using larger filled diamonds. The tension is apparently larger than that at $t=5$. For the case of $Dr=20$, A_e exhibits a periodic fluctuation, with a minimum at $t=5$ (see Fig. 5). This implies that the tension is correlated to the change in A_e , and therefore, that the smaller tension observed for $De=10^{-3}$ and $Dr=20$ may be attributed to the larger fluctuations in the cross section area. From the values given in Table I, we can see that the relative deviations in the tension, for the cases with $De=10^{-3}$, are significantly smaller than those with $De=10^{-2}$. As seen from Fig.9, the maximum deviation in the tension for $De=10^{-2}$ is located at the position closest to $x=0$, where the average configuration of the polymer chains is assumed to be isotropic, *i.e.*, all the components of the stress tensor are zero. Thus, we infer that the deviation near $x=0$ comes from the assumed initial configurations of the dumbbells. To obtain an initial configuration for the dumbbells without such an assumption, it is necessary to perform a multiscale simulation even at the up-stream side, including the die swell phenomenon, as well as inside the die, but this is outside the scope of the current work, and will be investigated in a future work.

Fig.10 shows the microscopic states of the dumbbells in Lagrangian particles located at three typical positions, (1) $x \approx 0.1$, (2) $x \approx 0.5$ and (3) $x \approx 1$ at $t=5$ for (a) $De=10^{-3}$ and (b) $De=10^{-2}$ in $Dr=15$. In the figures, a dot represents the posi-

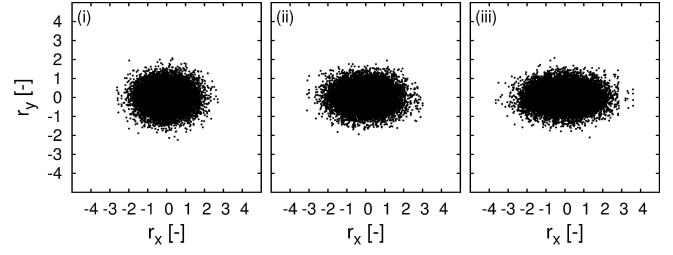


Fig. 11. Distribution of connecting vectors in a fluid particle located at $x \approx 1$ and at $t=5$ for $De=10^{-2}$ with (i) $Dr=10$, (ii) $Dr=15$ and (iii) $Dr=20$.

Table II. Conformation tensor $W_{\alpha\beta}$ at $x \approx 1$ for $De=10^{-3}$ and $De=10^{-2}$ for $Dr=$ (a) 10, (b) 15, (c) 20, (d) 25 and (e) 30.

Dr	De	W_{xx}	W_{yy}	W_{xy}	$-\sigma_{xx}/\sigma_{yy}$
(a) 10	10^{-3}	0.349	0.326	-2.89×10^{-5}	2.15
	10^{-2}	0.512	0.281	1.21×10^{-4}	3.39
(b) 15	10^{-3}	0.361	0.321	3.96×10^{-5}	2.23
	10^{-2}	0.675	0.258	9.55×10^{-5}	4.51
(c) 20	10^{-3}	0.374	0.316	2.43×10^{-5}	2.35
	10^{-2}	0.876	0.240	-4.06×10^{-5}	5.82
(d) 25	10^{-3}	0.390	0.311	-2.77×10^{-5}	2.48
	10^{-2}	1.11	0.227	-1.07×10^{-5}	7.32
(e) 30	10^{-3}	0.408	0.305	-1.94×10^{-5}	2.65
	10^{-2}	1.39	0.216	-7.26×10^{-5}	9.07

tion of one of the end points of a dumbbell, with the other end point fixed at the origin, where all of the end points within a single Lagrangian particle have been superimposed. From the figures, one can see the degree of deformation of the dumbbells due to the uni-axial elongational flow along the spinning line. In $De=10^{-3}$ (Fig.10(a)), the dots are almost isotropically distributed, although the distribution in (a-3) is slightly elongated along the flow direction. In (b) $De=10^{-2}$, on the other hand, the distribution at (2) $x \approx 0.5$ and (3) $x \approx 1$ is stretched along the x -direction, although the one at (1) $x \approx 0.1$ is almost isotropic. In particular, in (b-3) one can see that the dumbbells are largely elongated in the x -direction and shrunk in the y -direction. Fig.11 shows the distribution of connecting vectors in a Lagrange particle located at $x \approx 1$ at $t=5$ for different Dr with $De=10^{-2}$. From this Figure, we can see how the distribution is elongated as Dr increases.

Although we could qualitatively grasp the microscopic state of the dumbbells at typical positions, for various Deborah numbers and draw ratios, from Fig.10 and 11, in order to quantitatively understand the microscopic states of the system, we focus on the statistically averaged quantities describing the state of the dumbbells, such as their degree of stretching and orientation. For this purpose, we have analyzed the

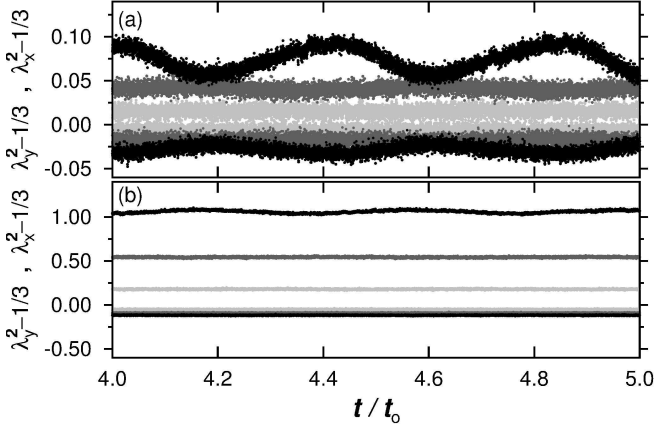


Fig. 12. Time evolutions of $\lambda_x^2 - 1/3$ and $\lambda_y^2 - 1/3$ at $x=1$ for $Dr=10$ (light grey), 15 (grey) and 20 (black) at (a) $De=10^{-3}$ and (b) $De=10^{-2}$. $\lambda_x^2 - 1/3$ and $\lambda_y^2 - 1/3$ are positive and negative, respectively.

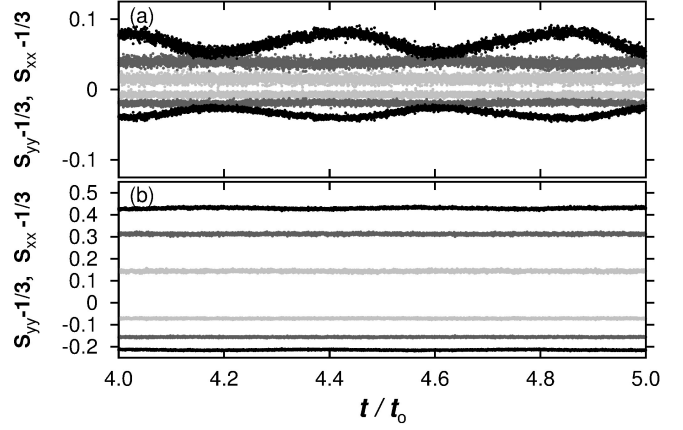


Fig. 13. Time evolution of S_{xx} and S_{yy} for $Dr=10$ (light grey), 15 (grey) and 20 (black) in (a) $De=10^{-3}$ and (b) $De=10^{-2}$. The xx - and yy -components are positive and negative, respectively.

conformation tensor $W_{\alpha\beta}$ defined as

$$W_{\alpha\beta} = \langle r_\alpha r_\beta \rangle = \frac{1}{N_p} \sum_{i=1}^{N_p} r_{i\alpha} r_{i\beta}. \quad (24)$$

It should be noted that this conformation tensor $W_{\alpha\beta}$ is related to the scaled stress tensor $\sigma_{\alpha\beta}$ of eq.(17). In Table II, we give W_{xx} , W_{yy} and W_{xy} at a position in the vicinity of $x=1$ at $t=5$ for $Dr=10, 15, 20, 25$ and 30 and $De=10^{-3}$ and 10^{-2} . The values of σ_{xx}/σ_{yy} at $x \approx 1$ are also shown in Table II. Given the axisymmetric geometry of the system, W_{zz} is statistically equal to W_{yy} . For the case of $Dr=10$ and 15 at $De=10^{-3}$, the xx - and yy -components are close to $1/3$, and xy -component is nearly zero, which means the state of the dumbbells is almost relaxed and isotropic. This result is consistent with Fig.10(a-3). In addition, σ_{xx}/σ_{yy} in these cases is close to -2 . Because $\sigma_{xx}/\sigma_{yy}=-2$ holds in an axis-symmetric flow of an incompressible Newtonian fluid, the state of the fluid throughout the spinning line can be approximated by that of a Newtonian fluid, on the other hand, for the other cases, the excess stress emerges. The conformation tensor $W_{\alpha\beta}$ can be decomposed into a stretch ratio λ and an orientation tensor $S_{\alpha\beta}$ as

$$W_{\alpha\beta} = \lambda^2 S_{\alpha\beta}, \quad (25)$$

where λ^2 is defined as the mean squared length of the dumbbells :

$$\lambda^2 = \text{Tr}(\mathbf{W}) = \sum_{\alpha=x,y,z} \lambda_\alpha^2 \quad (26)$$

with the stretch ratio in the α -direction given by:

$$\lambda_\alpha^2 = \frac{1}{N_p} \sum_{i=1}^{N_p} r_{i\alpha}^2. \quad (27)$$

In Fig.12 and Fig.13, we plot the time evolutions of the stretch ratio along the x - and y -directions, and the xx - and yy -components orientation tensor, respectively, for $Dr=10, 15$

and 20 at (a) $De=10^{-3}$ and (b) $De=10^{-2}$. When the macroscopic cross section area becomes smaller, the dumbbells are stretched along the flow direction, but shrunk in the perpendicular plane. As such, the stretch ratio $\lambda_x^2 - 1/3$ is strictly positive, and $\lambda_y^2 - 1/3$ negative. In addition, the xx -component of the orientation tensor is positive and the yy -component is negative for any parameter set, as expected from Fig.3. As shown in Fig.12, as the draw ratio becomes larger, the stretch ratio of the dumbbells along the flow direction λ_x becomes larger. We can see from Fig.12-13, that the stretch ratios, as well as the xx - and yy -components of the orientation tensor, for $Dr=20$ and $De=10^{-3}$, are temporally oscillating in phase with each other, and they are also synchronized with the change in A_e (for the corresponding parameter set shown in Fig.5). In the other cases, the stretch ratios and the orientation tensor show almost constant values, although they are rapidly fluctuating. From all these results, we can conclude that the larger relaxation time results in a more stable melt spinning process.

(b) Finite Re

As explained at the end of Sec.2.2, the typical Reynolds number in industrial spinning processes easily reaches values larger than 10^{-1} . Because the inertial effect cannot be ignored when solving the momentum equation (10) in this Re-regime, we use the scheme described in eq.(23) with $N_p=10^4$ dumbbells in each Lagrangian particle. In (b) Finite Re, the time increment Δt is set to $\Delta t=1.0 \times 10^{-5}$ for $Re=1.0$ and 0.1 , and $\Delta t=5.0 \times 10^{-6}$ or $\Delta t=1.0 \times 10^{-6}$ for $Re=0.01$. Fig.14 shows the time evolution of the cross section area $A_e(t)$ at $x \approx 1$. Despite performing simulations for the eighteen different combinations of the following parameters $Dr=10, 20, 30$, $Re=10^{-2}, 10^{-1}, 1$ and $De=10^{-3}, 10^{-2}$, the resulting values for the relative cross section areas all converge to three lines, depending only on the $Dr=10, 20, 30$; with smaller Dr corresponding to larger A_e , as shown in in Fig.14. While the cases for $Dr \gtrsim 20$ and $De=10^{-3}$ at $Re \ll 1$ exhibit the draw resonance phenomenon, the flow and cross section area in the present

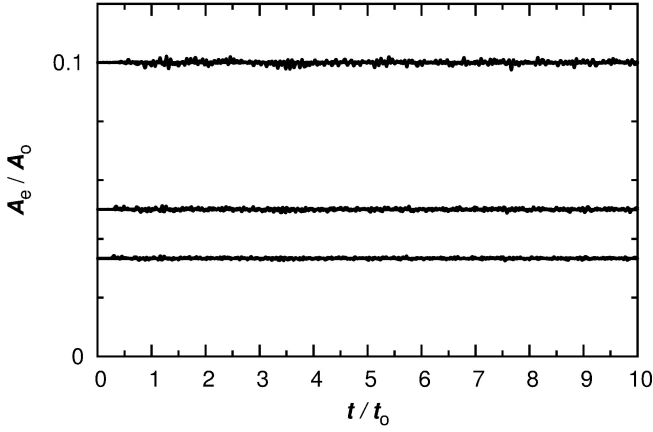


Fig. 14. Time evolution of the cross section area A_e at the end point ($x=1$), for the eighteen combinations of $Dr=10, 20, 30$, $Re=10^{-2}, 10^{-1}, 1$ and $De=10^{-3}, 10^{-2}$. The results all converge into three lines, depending only on the draw ratio, $Dr=10$ (top), 20 (middle), 30 (bottom).

case are quite stable, even at $Dr=30$ for $De=10^{-3}$. We have found that the inertial effects make the spinning process stable, in addition to the elastic effect.

In Fig.15, we separately show the velocity profiles for (a) $Re=10^{-2}$ and (b) 10^{-1} and 1 . For each Reynolds number, we plot the data obtained for the six following parameter combinations: $Dr=10$ (circle), 20 (diamond), 30 (triangle), and $De=10^{-3}$ (open symbols) and 10^{-2} (filled symbols). In addition, the results obtained by using the Maxwell constitutive equation are plotted by solid lines. As seen from the figures, the velocity profiles for $Dr=10$ are irrespective of De and Re . At $Dr=20$ and 30 , the velocity profiles are almost the same, except for the case with $Re=10^{-2}$ and $De=10^{-3}$ (open triangles in (a)) whose velocity profile deviates towards higher values. From these results, the velocity profiles for $Re \gtrsim 10^{-1}$ seem to depend only on the draw ratio. In Fig.16 we show the profiles of the cross section area at $t=10$ for $Dr=10, 20, 30$ and $De=10^{-3}, 10^{-2}$ at (a) $Re=10^{-2}$ and (b) $Re=10^{-1}$ and 1 . All the profiles for $Dr=10$ in (a) are on the same line, *i.e.*, they are independent of De . The profiles for $Dr=20$ and 30 , on the other hand, depend on De , and the cross section areas for larger De becomes thinner, particularly near the center region. In (b), the area profiles depend only on the draw ratios, which is consistent with the results of the velocity profiles at $Re \gtrsim 10^{-1}$ shown in Fig.15. As with the low Reynolds number limiting case shown in Fig.6, the distribution of Lagrangian particles on the spinning line is a monotonically decreasing function of x . This is because the density of particles is proportional to the inverse of the velocity. Since the stress tensor at a Eulerian grid point is evaluated by averaging over the stress tensors of the Lagrangian particles located within a spatial interval of width Δx , a larger number of particles will always increase the statistical accuracy and improve the numerical stability. In the present simulation, a new particle is inserted at $x=0$, so that at least twenty Lagrangian particles always exist in the region closest to $x=1$, as seen in Fig.17. The total numbers of

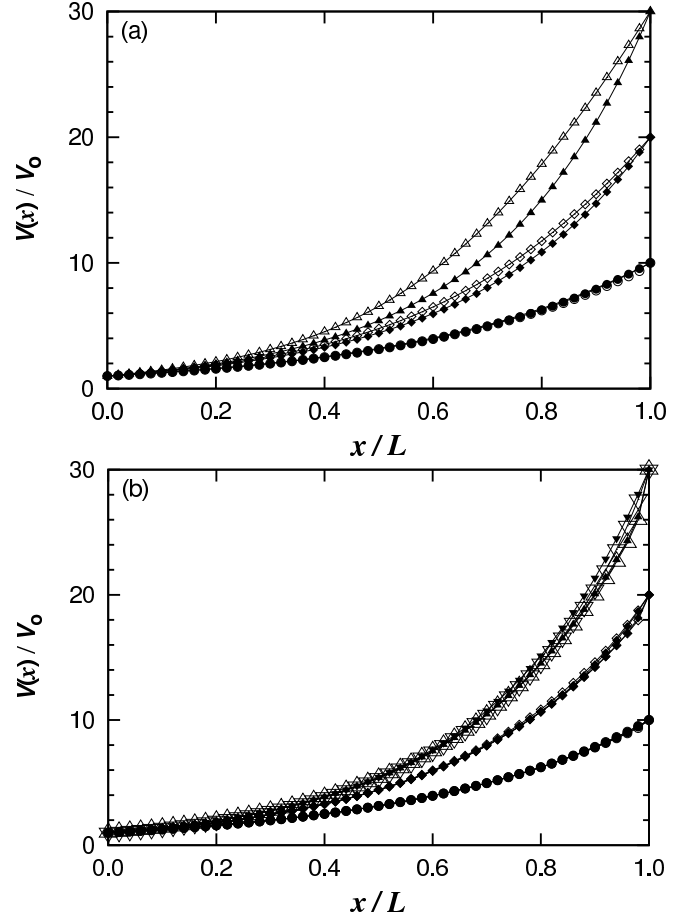


Fig. 15. Velocity profiles at $t=10$ for (a) $Re=10^{-2}$ and (b) 10^{-1} and 1 . The six combinations of the three draw ratios $Dr=10$ (circle), 20 (diamond), 30 (triangle) and two Deborah numbers $De=10^{-3}$ (filled symbol) and 10^{-2} (open symbol) are plotted for each Re . In (b), triangle symbols for $Re=10^{-1}$ and $Re=1$ are distinguished by using lower and upper triangles, respectively. Namely, the velocity close to $x=1$ for $Re=10^{-1}$ is slightly higher than that for $Re=1$. The solid lines are the velocity profiles obtained by using the Maxwell constitutive equation with the parameters corresponding to the nearest symbols.

Lagrangian particles in the steady state, for $Dr=10, 20$ and 30 , are $N_L^{(Total)} \simeq 7850, 10600$ and 19100 , respectively.

As with Fig.10, in Fig.18 we show the distribution of one of the two end points for dumbbells belonging to Lagrangian points located at (1) $x \simeq 0.1$ (2) $x \simeq 0.5$ and (3) $x \simeq 0.9$, at $t=10$, for $Re=1$ and $Dr=30$ at (a) $De=10^{-3}$ and (b) 10^{-2} . In (a) $De=10^{-3}$, the state of the dumbbells at $x \simeq 0.1$ and 0.5 are almost isotropic, but the state at $x \simeq 0.9$ is slightly stretched along the flow direction. In (b) $De=10^{-2}$, on the other hand, one can see that the state of the dumbbells is deformed from the isotropic state even at $x \simeq 0.1$, and at $x \simeq 0.9$ the dumbbells are highly stretched along x -direction and compressed in the y -direction, as seen in (b-3). Fig.19 shows the distribution of connecting vectors in a Lagrangian particle located at $x \simeq 0.9$ at $t=10$ for the nine combinations of $Re=10^{-2}, 10^{-1}, 1$ and $Dr=10, 20, 30$ in $De=10^{-2}$. The distributions are almost the

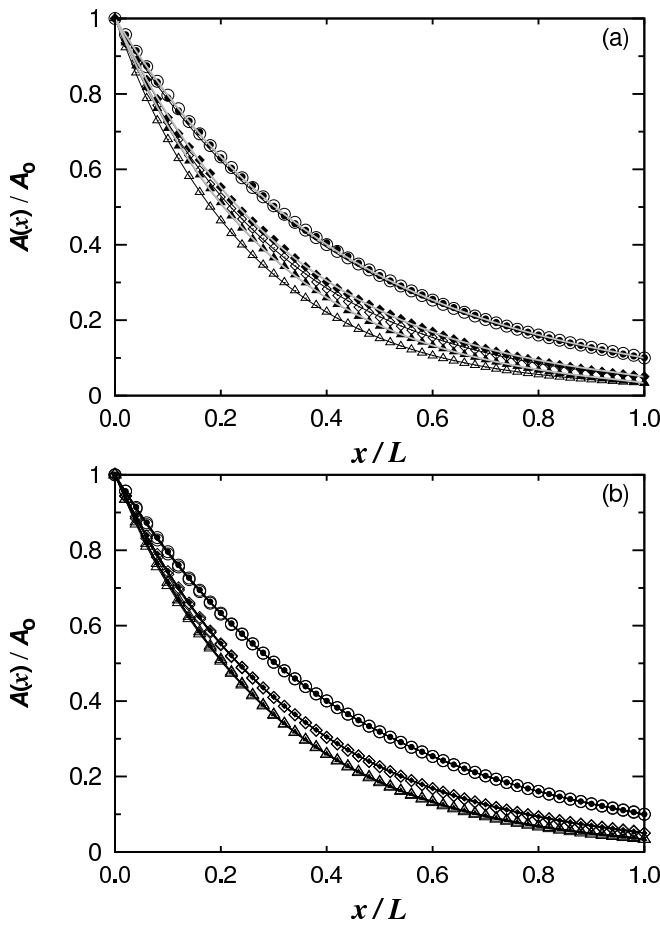


Fig. 16. Cross section area as a function of position on the spinning line, at $t=10$, for $Dr=10$ (circle), 20 (diamond), 30 (triangle) and $De=10^{-3}$ (open symbol), 10^{-2} (filled symbol) at (a) $Re=10^{-2}$ and (b) $Re=0.1$ and 1. The solid lines (in (a) white and (b) black colors) are the results obtained by using Maxwell constitutive equation with the parameters corresponding to the symbols.

same if the draw ratio Dr is the same, except for (i-1) $Re=10^{-2}$ and $Dr=10$. This result also means that the state of the dumbbells is determined only by Dr if Re is large enough, which is consistent with the results shown in Figs.15 and 16, where the velocity and cross section area converge towards profiles depending only on Dr .

4. Summary

In the present study, we applied a multiscale simulation method to a melt spinning processes. In the simulations, we use a dumbbell model as the microscopic model for the polymer chains in order to validate our multiscale simulation method. Based on the fact that the stress evaluated by the statistical average of a set of dumbbells is mathematically equivalent to the one calculated from the Maxwell constitutive equation, we can directly assess the accuracy of our multiscale simulation method, by comparing our results for the microscopic model, with those obtained using the corresponding constitutive equation. Actually, the validation of the mul-

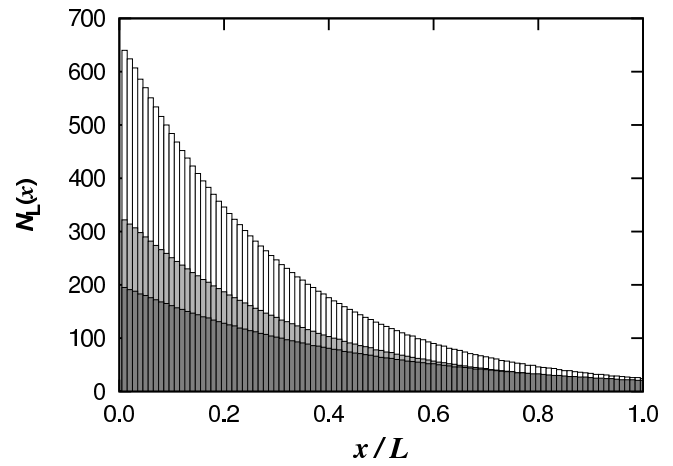


Fig. 17. Typical histogram of the number of Lagrangian particles $N_L(x)$ existing in the spatial interval $[x, x + \Delta x]$ along the spinning line at $t=10$, for $Dr=10$ (dark grey), 20 (light grey), 30 (white).

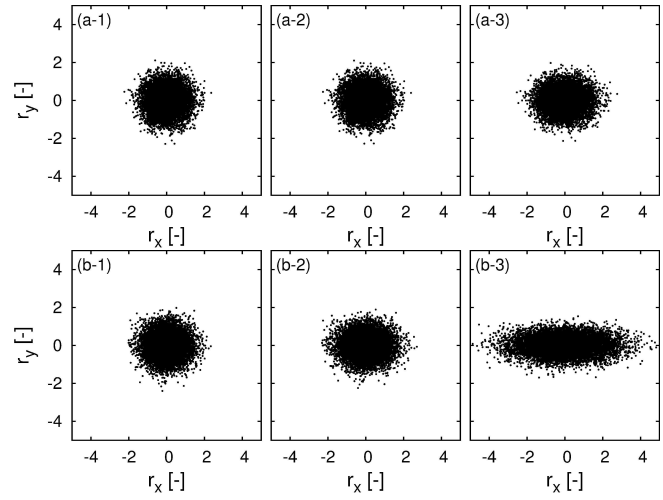


Fig. 18. Distribution of connecting vectors in a Lagrangian particle located at (1) $x \approx 0.1$, (2) 0.5 and (3) 0.9 for (a) $De=10^{-3}$ and (b) $De=10^{-2}$ in $Dr=30$ and $Re=1$.

tiscale simulation method is of particular importance, because the method itself is still under development. The schemes used to solve the momentum equation are chosen depending on the Reynolds number, *i.e.*, (a) $Re \rightarrow 0$ and (b) finite Re . In the limit (a), the tension balance always holds along the spinning line, and the Broyden method is used to evaluate the velocity. We found that the elastic effect and a longer relaxation time improve the stability of the spinning process, and that the draw resonance phenomenon that takes place above $Dr \approx 20.21$ in the Newtonian fluid, is suppressed at $De=10^{-2}$, at least up to $Dr=30$. In the limiting case in (b), on the other hand, the inertia effect starts to play an important role in determining the dynamical behavior of the spinning process above $Re \approx 10^{-1}$. In this Re -regime, the spinning process is quite stable, and the profiles for the cross section area and velocity along the

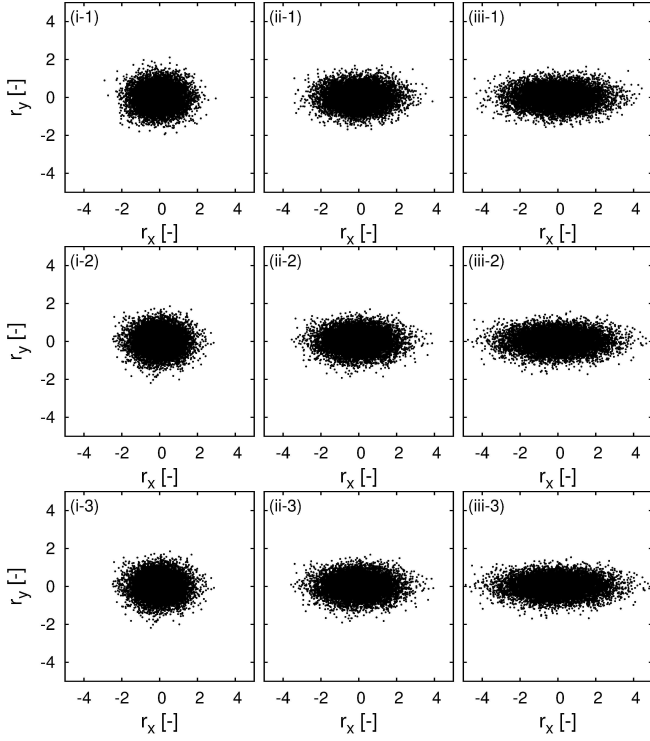


Fig. 19. Distribution of connecting vectors in a Lagrangian particle at $x=0.9$ and at $t=10$ for (i) $Re=10^{-2}$, (ii) $Re=10^{-1}$, and (iii) $Re=1$, and (1) $Dr=10$ (2) $Dr=20$ and (3) $Dr=30$ in $De=10^{-2}$.

spinning line are determined only by the draw ratio Dr . In both cases (a) and (b), we used N_p -dumbbells ($N_p=10^4$) in a Lagrangian particle. The use of a finite number of dumbbells in a Lagrangian particle always brings with it a non-zero statistical error for the computed stress, as compared to the one obtained by the Maxwell constitutive equation. Even though the number of dumbbells in a Lagrangian particle is $N_p=10^4$ in this work, the present scheme gives good agreement with the results obtained by the Maxwell constitutive equation. In addition, we demonstrated that the MSS method is useful in bridging the macroscopic behavior and the simultaneous microscopic state, by comparing the velocity and cross section area profiles with the end point distribution of the connecting vectors for the dumbbells in a Lagrangian particle at characteristic locations along the spinning line.

We hope that the MSS method we propose brings us to a new stage in the field of material science, by allowing us to develop novel approaches in designing materials. In particular, we hope to increase the current understanding of the flow behaviors of polymeric materials, not only from a macroscopic point of view, but also from a detailed microscopic level.

In the near future, by employing a more realistic microscopic model for the polymer chains, such as the primitive chain network models (PASTA^{28,29}, NAPLES²⁶), an improved description of the entanglements of the polymer chains and their orientations will be incorporated into our MSS method. In the present work, we have simply used an isother-

mal condition. However, in many industrial problems, the temperature is not homogeneous and a solidification and/or a crystallization of the polymeric material may occur. To deal with such phenomena, we need to extend the microscopic model or even develop a new one. In addition, to overcome the problems due to the high computational cost, we will have to improve the numerical schemes, including the parallelization of the numerical codes. Thereby, the MSS method will be more effective in solving problems with industrial applications.

The authors would like to express our sincere gratitude to J. Molina for giving valuable comments and for kindly proof-reading the present paper. This work was supported partially by JSPS KAKENHI Grant Number 15K13549 and by the FLAGSHIP2020, MEXT within the challenging study, sub-theme B.

Appendix: Analytic Solutions of steady state at limits

We need to rely on a numerical method to obtain a steady state solution of eqs.(7)-(11) and (18) at a finite Deborah number, but in the two limits: (I) $De \rightarrow 0$ and (II) $De \rightarrow \infty$, one can obtain analytic solutions for the steady states.

(I) $De \rightarrow 0$ (Newtonian limit)

The analytic solution of the steady state for the spinning process of a Newtonian fluid at $Re \neq 0$ can be obtained as

$$V(x) = Dr \frac{Re - (Re - C)e^{Cx/3}}{Re - (Re - C)e^{Cx/3}}, \quad A(x) = [V(x)]^{-1} \quad (A.1)$$

with the constant C determined by the following equation:

$$C + Dr(Re - C)e^{Cx/3} = DrRe. \quad (A.2)$$

The tension F is given by

$$F(x) = \frac{C(Re - C)e^{Cx/3}}{Re - (Re - C)e^{Cx/3}}. \quad (A.3)$$

If one takes the limit $Re \rightarrow 0$, the constant C is found to be $-3 \ln(Dr)$, and the above analytic solution turns out to be the well-known analytic solution at the steady state ($Dr < 20.21$)^{8,12} of the spinning process for a Newtonian fluid with $Re=0$ as

$$V(x) = (Dr)^x, \quad A(x) = (Dr)^{-x}, \quad F = 3 \ln(Dr). \quad (A.4)$$

(II) $De \rightarrow \infty$ (Elastic limit)

In the elastic limit ($De \rightarrow \infty$), one can also obtain the analytic solution as

$$V(x) = 1 + (Dr - 1)x, \quad A(x) = [1 + (Dr - 1)x]^{-1}. \quad (A.5)$$

The elastic stresses for xx -, yy - and zz -components are

$$\sigma_{xx} = ReDr^2 \frac{Dr - 1}{Dr^3 - 1} [V(x)]^2 \quad (A.6)$$

$$\sigma_{yy} = \sigma_{zz} = \frac{1}{2} ReDr^2 \frac{Dr - 1}{Dr^3 - 1} [V(x)]^{-1}. \quad (A.7)$$

Then the tension is given as

$$F = \text{ReDr}^2 \frac{\text{Dr} - 1}{\text{Dr}^3 - 1} [V(x) - V(x)^{-2}]. \quad (\text{A-8})$$

- 1) H. Ishihara, *Seikei-Kakou*, **23**, 276-285 (2011) in Japanese.
- 2) H. Ishihara, *Seikei-Kakou*, **23**, 336-346 (2011) in Japanese.
- 3) H. Ishihara, *Seikei-Kakou*, **23**, 430-440 (2011) in Japanese.
- 4) S. Kase and T. Matsuo, *J. Polym. Sci. Part A*, **3**, 2541 (1965).
- 5) S. Kase and T. Matsuo, *J. Polym. Sci. Part A*, **11**, 251 (1967).
- 6) M. A. Matovich and J. R. A. Pearson, *Ind. Eng. Chem. Fund.*, **8**, 512-520 (1969).
- 7) J. R. A. Pearson and M. A. Matovich, *Ind. Eng. Chem. Fund.*, **8**, 606 (1969).
- 8) D. Gelder, *Ind. Eng. Chem. Fund.*, **10**, 534 (1971).
- 9) Y. T. Shah and J.R.A.Pearson, *Ind.Eng. Chem. Fund.* **11** 150, (1972).
- 10) H. Ishihara and S. Hayashi, *Nihon Reoroji Gakkaishi*, **17**, 19 (1973) in Japanese.
- 11) M. M. Denn and C. J. S. Petrie, *AIChE J.*, **21**, 791 (1975).
- 12) R. J. Fisher and M. M. Denn, *Chem. Eng. Sci.*, **30**, 1129 (1975)
- 13) H. Ishihara, *J. Appl. Polym. Sci.*, **20**, 169 (1976).
- 14) J. C. Hyun, *AIChE J.* **24**, 423 (1978).
- 15) H. Ishihara and S. Hayashi, *Nihon Reoroji Gakkaishi*, **17**, 19 (1989)
- 16) H. Ishihara, S. Hayashi and H. Yasuda, *Nihon Reoroji Gakkaishi*, **20**, 109 (1992), in Japanese.
- 17) H. Ishihara, M. Shibata and K. Ikeda, *Nihon Reoroji Gakkaishi*, **34**, 3 (2006), in Japanese.
- 18) W. Takarada *et al*, *Journal of Applied Polymer Science*, **80**, 1589 (2001).
- 19) J. H. Yun, *Nihon Reoroji Gakkaishi*, **36** 133 (2008).
- 20) S. S. N. Perera, *Nihon Reoroji Gakkaishi*, **36**, 161 (2008).
- 21) R. Dhadwal, *Applied Mathematical Modelling*, **35**, 2959 (2011).
- 22) P. E. Rouse, *J. Chem. Phys.*, **21**, 1272 (1953).
- 23) R. B. Bird, R. C. Armstrong, and O. Hassager, *Dynamics of polymeric liquids* Vol. 1 and 2 (John Wiley & Sons, New York, 1987).
- 24) K. Kremer and G. S. Grest, *J. Chem. Phys.*, **92**, 5057 (1990).
- 25) M. Doi and S. F. Edwards, *The theory of polymer dynamics.*, (Oxford University Press, New York, 1986).
- 26) Y. Masubuchi *et al*, *J. Chem. Phys.*, **115**, 4387 (2001).
- 27) S. Shanbhadg *et al*, *Phys. Rev. Lett.*, **87**, 195502 (2001).
- 28) H. Tasaki, J. Takimoto and M. Doi, *Comput. Phys. Commun.*, **142**, 136, (2001).
- 29) M. Doi and J. Takimoto, *Phil. Trans. R. Soc. Lond.*, **A 361**, 641 (2003).
- 30) J. D. Schieber, J. Neergaard, and S. Gupta, *J. Rheol.*, **47**, 213 (2003).
- 31) A. E. Likhtman, *Macromolecules*, **38**, 6128 (2005).
- 32) H. C. Öttinger, *Beyond Equilibrium Thermodynamics* (Wiley-Interscience, New Jersey, 2005).
- 33) M. Laso and H. C. Öttinger, *J. Non-Newtonian Fluid Mech.*, **47**, 1 (1993).
- 34) K. Feigl, M. Laso, and H. C. Öttinger, *Macromolecules*, **28**, 3261 (1995).
- 35) L. E. Wedgewood and K. R. Geurts, *Ind. Eng. Chem. Res.*, **34**, 3437 (1995).
- 36) C. C. Hua and J. D. Schieber, *Chem. Eng. Sci.*, **51**, 1473 (1996).
- 37) A.P.G. van Heel *et al*, *J. Non-Newtonian Fluid Mech.*, **75**, 253 (1998).
- 38) M. Laso, M. Picasso and H. C. Öttinger, *AIChE J.*, **43**, 877 (1997).
- 39) P. Halin *et al*, *J. Non-Newtonian Fluid Mech.*, **79**, 387 (1998)
- 40) J. Bonvin and M. Picasso, *J. Non-Newtonian Fluid Mech.*, **84**, 191 (1999)
- 41) W. Ren and W. E, *J. Comput. Phys.*, **204**, 1 (2005).
- 42) W. E, *et al*, *Commun. Comput. Phys.*, **2**, 367 (2007).
- 43) S. Yasuda and R. Yamamoto, *Phys. Fluids*, **20**, 113101 (2008).
- 44) S. Yasuda and R. Yamamoto, *Europhys. Lett.*, **86**, 18002 (2009).
- 45) S. Yasuda and R. Yamamoto, *Phys. Rev. E*, **81**, 036308 (2010).
- 46) S. Yasuda and R. Yamamoto, *Phys. Rev. E*, **84**, 031501 (2011).
- 47) T. Murashima and T. Taniguchi, *J. Polym. Sci. B*, **48**, 886 (2010).
- 48) T. Murashima and T. Taniguchi, *Europhys. Lett.*, **96**, 18002 (2011).
- 49) T. Murashima and T. Taniguchi, *J. Phys. Soc. Jpn.*, SA013 (2011).
- 50) T. Murashima *et al*, *J. Phys. Soc. Jpn.*, **82**, 012001 (2013).
- 51) If one wants to simulate industrial melt spinning processes, the isothermal assumption should be replaced by a non-isothermal one, but we are considering that the ideal isothermal condition is suitable to make an assessment of the present multiscale simulation.
- 52) The time period t^* is estimated by $t^* = \int_0^1 dx/V(x)$ and $V(x)$ in (A-4).
- 53) In the present works, (i) 24Cores: Xeon E5-1680v3 (3.2GHz) and (ii) 16Cores: Xeon E5-2680 (2.7GHz) are used in (a), and the CPU (i) is used in (b).